ACS APPLIED ENERGY MATERIALS

www.acsaem.org Article

Hierarchical MoS_2 Nanotubes Supported by Tubular CoS_2 on Carbon Cloth as Flexible Electrodes for Durable Lithium-Ion Storage

Shenyu Du, Liyuan Ao, Jianli Tang, Kai Jiang, Liyan Shang, Yawei Li, Jinzhong Zhang, Liangqing Zhu,* Zhigao Hu,* and Junhao Chu

Cite This: *ACS Appl. Energy Mater.* 2022, 5, 10056−10066 Read Online

ACCESS | Metrics & More | Article Recommendations | Supporting Information

ABSTRACT: An ingenious design and a controllable architecture are critical for the construction of flexible electrodes. In this study, we realized the enriched nanorods on carbon cloth as templates by controlling the growth of metal−organic frameworks (MOFs) and finally formed hollow CoS_2@MoS_2 nanotube arrays after postprocessing. The outer layer is staggered interconnected MoS_2 nanosheets with gaps between them, providing rich active points for electrochemical reaction. The hierarchical tubular structure and core−shell system significantly improves the electrical conductivity, promotes the diffusion of lithium ions, and has a good buffering effect on the volume change. Therefore, it exhibits an excellent lithium storage capacity with an areal specific capacity as high as 2.35 mAh cm^{-2} after 100 cycles at a current density of 0.5 mA cm^{-2}. Furthermore, it reaches 1.55 mAh cm^{-2} in the full-cell test at 5 mA cm^{-2}. At the same time, its strong flexibility enables stable capacity output in pouch cells. In this regard, our research provides an idea for the application of flexible devices.

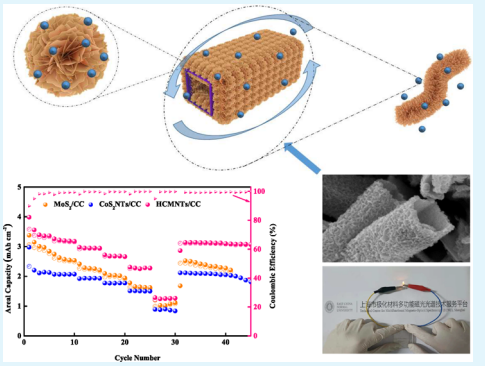

KEYWORDS: *MoS_2, CoS_2, core−shell, carbon cloth, lithium-ion battery*

1. INTRODUCTION

Lithium-ion batteries (LIBs) have made great progress in the application of energy conversion and energy storage devices due to their high safety, long cycle life, and high energy density.[1−4] However, research on flexible lithium-ion batteries is still in its infancy.[5] As portable electronic devices show a trend of gradual miniaturization and high integration, the applications and demands of flexible electronic devices in communications, medical treatment, and wearable consumer electronics are increasing.[6−9] As the energy source in these flexible electronic devices, high-performance flexible batteries play an indispensable role. Compared with traditional LIBs, flexible LIBs not only contain all of the functional properties of traditional batteries but also need to have the characteristics of foldability, lightweight, stretchability, and implantability.[10] Traditional battery electrodes are usually made by mixing active materials with conductive carbon additives and polymer binders and then coating the mixture on metal foils. However, the flexibility of this electrode is largely limited by the metal current collector, and it is difficult for the current collector to restore its original shape after being folded or deformed.[11] Correspondingly, the method of directly using flexible current collectors (carbon cloth, carbon paper) likely causes the active material to detach under deformation due to insufficient adhesion, resulting in a serious degradation of the cycle life.

To enhance the interaction between them, a more effective method is to directly grow active materials on flexible substrates.[12−14] To date, carbon-based conductive substrates such as carbon nanotube (CNT) paper,[15] carbon cloth (CC),[16] graphene,[17] and MXene[18] have been widely studied. Among them, CC has been studied for its commercial value as well as strong conductivity, high stability, and good electrochemical characteristics. The staggered carbon network structure has rich pores, which improves electrolyte prestorage and significantly enhances ion diffusion and transport.[19,20] However, the specific capacity of carbon cloth as an anode is relatively low (~90 mAh g^{-1}), so it needs to be effectively combined with other active materials. Currently, molybdenum disulfide (MoS_2) has attracted much attention because of its unique layered structure and weak interlayer van der Waals force. As the intercalation host material of lithium ions, the layer spacing (0.62 nm) of MoS_2 is larger than that of graphite (0.335 nm), and lithium ions are easier to diffuse without significant volume change.[21,22] During the electrochemical reaction, the alternately connected S−Mo−S structure provides active sites for the insertion and storage of Li_2S and Mo, resulting in a high theoretical capacity (669 mAh g^{-1}).[23,24]

Received: May 30, 2022
Accepted: July 28, 2022
Published: August 11, 2022

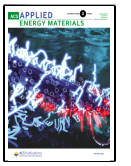

https://doi.org/10.1021/acsaem.2c01675
ACS Appl. Energy Mater. 2022, 5, 10056−10066

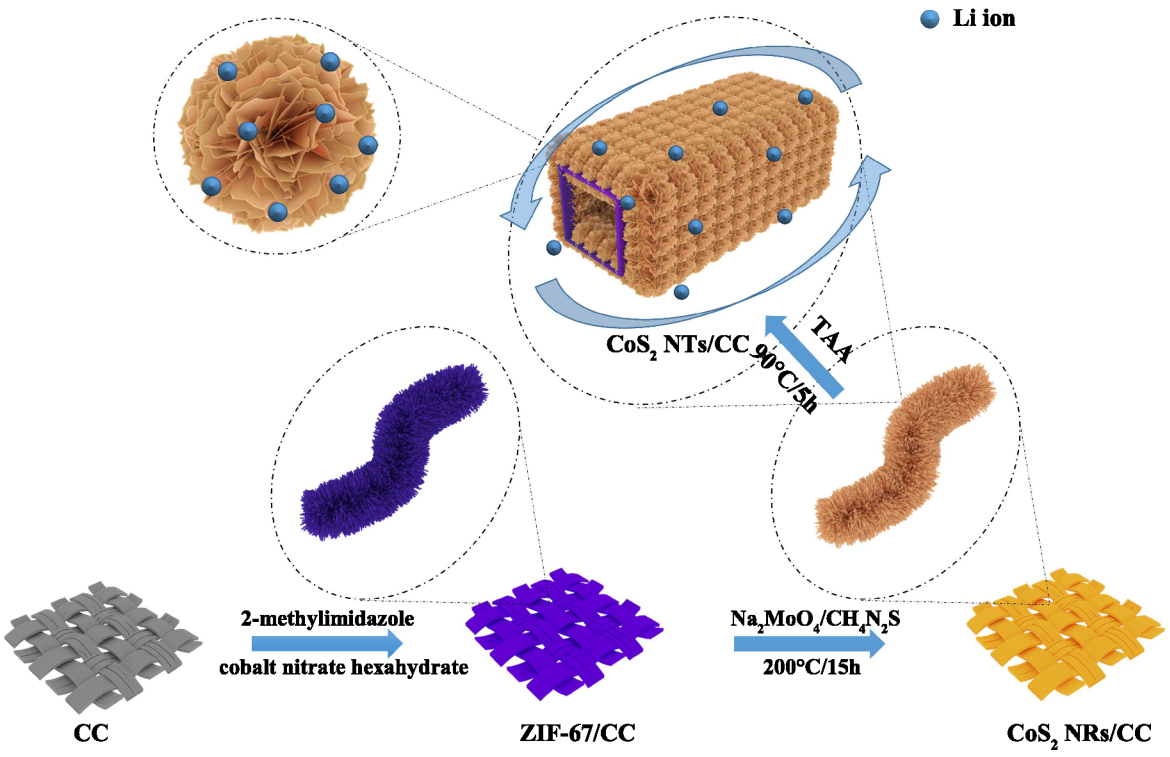

Figure 1. Synthesis route of hollow core−shell structure CoS_2@MoS_2 on carbon cloth, and schematic diagram of its lithium-ion storage process.

Therefore, a lot of research has been carried out on MoS_2-based materials as anodes of LIBs. For example, Yu and his coauthor synthesized 3D graphene/MoS_2 nanosheet arrays on the surface of carbon cloth. The structure has a large specific surface area and porous characteristics, and the specific capacity can still reach 516 mA h g^{-1} at a current density of 8 A g^{-1}. Although this scheme has achieved high capacity performance, the uncovered MoS_2 was easily detached from the substrate during the cycle, resulting in poor cycle performance.[25] Considering the limitations of the large mass and small specific surface area of carbon cloth, the design of MoS_2 with a specific structure can effectively improve the stability of flexible LIBS. Therefore, Deng et al. prepared 3D-ordered macroporous MoS_2/carbon nanocomposites for Li-ion storage. The pores are regularly embedded in interconnected carbon walls to supply a large specific surface area and space. The constructed high-performance foldable flexible electrode can provide a high discharge capacity of 3.428 mAh cm^{-2} at a rate of 0.1 mA cm^{-2}.[26] Furthermore, our previous work demonstrated the synthesis method of the CoS_2@MoS_2 core−shell structure anchored on carbon cloth. The porous MoS_2 nanoarray on the surface increases the contact area for the reaction, and the core−shell structure can effectively solve the volume change and agglomeration of MoS_2 during cycling, which causes the electrode to discharge a specific capacity as high as 1175 mAh g^{-1} at a current density of 0.1 A g^{-1}. At the same time, the structure improves the stability of electrochemical reaction, which greatly prolongs the service life of the battery.[27]

Here, we synthesized ZIF-67 nanoarrays as templates followed by hydrothermal and etching methods to obtain hierarchical CoS_2@MoS_2 nanotube arrays on carbon cloth (HCMNTs/CC) as flexible electrodes for lithium-ion storage. In this process, the metal−organic framework (MOF) nanorod array on the carbon cloth can not only be subsequently vulcanized into CoS_2 but also serve as a template for the hollow structure. At the same time, the characteristics of carbon cloth are reasonably used to improve the overall conductivity of the electrode. As expected, the obtained hollow nanotube arrays increase the reaction area with the electrolyte, which promotes the transport of electrons and the diffusion of ions. In addition, introduction of CoS_2 improves the electrical conductivity, resulting in a higher electrochemical performance. Due to the existence of the core−shell composite structure, the volume change of the electrode in the process of charge and discharge is alleviated and sufficient active sites are provided. The prepared binder-free flexible electrode was directly used as a lithium-ion battery anode, exhibiting a high areal specific capacity of 2.35 mAh cm^{-2} at 0.5 mA cm^{-2} and an enhanced rate capability of 1.27 mAh cm^{-2} at 5 mA cm^{-2}. This scheme provides a new possibility for the realization of wearable flexible energy devices.

2. EXPERIMENTAL SECTION

Materials Preparation. The carbon cloth (WOS1011) was ultrasonically cleaned with acetone, deionized water, and alcohol for 15 min to remove impurities. After drying, it was treated with oxygen plasma (air, 50 W, 0.3 Torr) to improve its hydrophilicity. To generate ZIF-67 nanoarrays on CC, 1.642 g of 2-methylimidazole and 0.364 g of cobalt nitrate hexahydrate were respectively dissolved in 25 mL of deionized water and stirred for 15 min before mixing. Then, a piece of pretreated carbon cloth (3 cm × 6 cm) was quickly immersed into the mixed solution. After 8 h of reaction, the samples were taken out, washed with deionized water, and dried in an oven overnight.

The prepared ZIF-67 NRs on CC (3 cm × 3 cm) were immersed in 30 mL of a DMF homogeneous solution containing 0.15 mmol of Na_2MoO_4 and 0.82 mmol of thiourea. The solution was then transferred to a 50 mL Teflon-lined stainless steel autoclave and sealed at 200 °C for 15 h. The obtained product was washed with water and ethanol several times and dried in an oven for 12 h. The CC was then immersed in 30 mL homogeneous aqueous solution

https://doi.org/10.1021/acsaem.2c01675
ACS Appl. Energy Mater. 2022, 5, 10056−10066

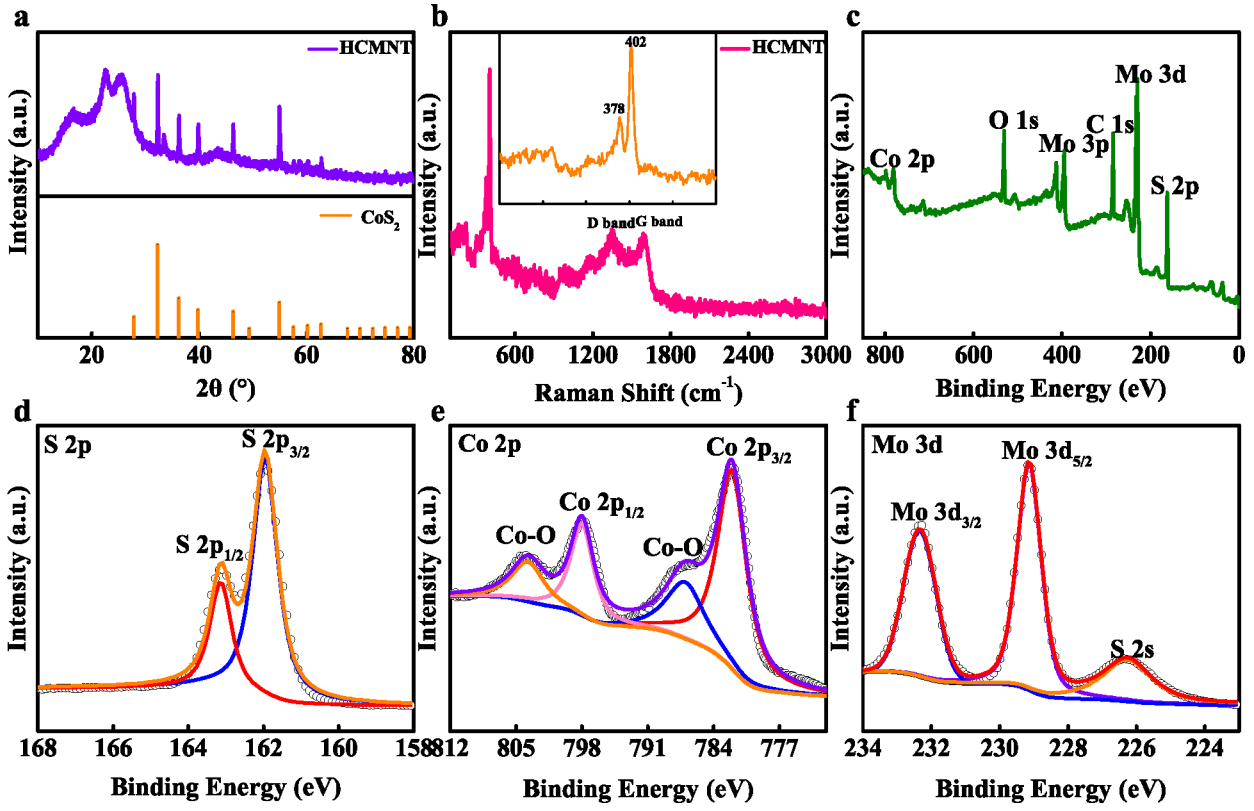

Figure 2. (a) XRD pattern of the as-prepared HCMNTs/CC. (b) Raman spectra of the as-prepared HCMNTs/CC. (c) XPS spectrum of HCMNTs/CC. High-resolution scans of (d) S 2p, (e) Co 3d, (f) and Mo 2p.

dispersed with 160 mg of thioacetamide (TAA) and transferred together into a Teflon-lined stainless steel autoclave (50 mL). The sample was kept at 90 °C for 5 h and removed after cooling to room temperature naturally. It was washed with deionized water and ethanol, dried overnight, and then annealed for 2 h at 500 °C in an Ar atmosphere. The average mass of the HCMNTs loaded on the CC was about 3.03 mg cm^{-2}.

Materials Characterization. Scanning electron microscopy (SEM) images and transmission electron microscopy (TEM) images were acquired using a Philips XL30TMP system and a FEI Tecnai G2 F20 TEM at an experimental voltage of 200 kV to facilitate analysis of the morphology and structure of the samples. X-ray diffraction (XRD) analysis was carried out on Bruker D8 Advance diffractometer with Cu Kα radiation (λ = 1.5418 Å) at a 2θ range from 10° to 80°. The chemical properties of the samples were analyzed by X-ray photoelectron spectroscopy (XPS) (PHI5000C ESCA, Mg Kα radiation with $h\nu$ = 1253.6 eV) and Raman spectroscopy (Jobin Yvon LabRAM HR 800, 532 nm). ICP-OES elemental analysis was performed on an Agilent 730 ICP-OES spectrometer.

Electrochemical Measurement. The CR2025 coin-type half-cell was assembled in a glovebox filled with argon. The prepared flexible electrode was cut into a fixed size (d = 12 mm) and directly used as the working electrode, while lithium foil was used as the counter electrode. $LiPF_6$ (1 M) dispersed in ethylene carbonate/dimethyl carbonate/diethyl carbonate (EC/DMC/DEC) was used as the electrolyte with a volume ratio of 1:1:1. Celgard 2400 membrane was used as the separator. Cyclic voltammetry (CV) curves at rates from 0.1 to 10 mV/s were tested on a CHI660E electrochemical workstation, and electrochemical impedance spectroscopy (EIS) was studied in the frequency range from 0.01 Hz to 100 kHz. The galvanostatic charge−discharge performance in the voltage range of 0.01−3.0 V (vs Li^+/Li) was carried out on the Land battery test station. The soft pack battery was assembled with the prepared HCMNTs on CC as the anode and commercial $LiCoO_2$/Al as the cathode. Electrochemical tests were performed in the potential window range from 1.0 to 4.2 V.

3. RESULTS AND DISCUSSION

Figure 1 shows the process of preparing hollow core−shell CoS_2@MoS_2 by solution deposition of ZIF-67 nanorod arrays on carbon cloth and further in situ vulcanization and etching. First, the pretreated carbon cloth was vertically immersed in a ZIF-67 suspension for static reaction. Purple nanorod arrays can grow evenly on the surface of carbon cloth because its surface is rich in oxygen-containing functional groups.[28] Actually, the ZIF-67-based nanostructure arranged on the carbon cloth can be effectively controlled by changing the experimental temperature and solution concentration.[29] Then, two-dimensional (2D) MoS_2 nanosheets were deposited on the surface of the nanorods by hydrothermal reaction of sodium molybdate and thiourea. In this process, the excess S ions provided by thiourea combine with the Co ions in the nanoarray to form in situ CoS_2 as the skeleton, provide active sites for the growth of MoS_2, and finally form a core−shell structure. It can be seen that the dual effects of the Kirkendall effect and anion exchange promote the faster diffusion of Co ions to form CoS_2.[30] At the same time, the core−shell structure of CoS_2@MoS_2 is constructed with high efficiency.[31,32] Finally, CoS_2 can be further deposited and etched with the promotion of TAA to form hierarchical CoS_2@MoS_2 nanotube arrays.

As shown in the enlarged inset of Figure 1, the staged reaction finally builds a robust intercalation and desorption system of lithium ions. The construction of nanoarrays on the surface of carbon cloth significantly increased the surface area of the substrate, and the molybdenum sulfide was anchored

https://doi.org/10.1021/acsaem.2c01675
ACS Appl. Energy Mater. 2022, 5, 10056−10066

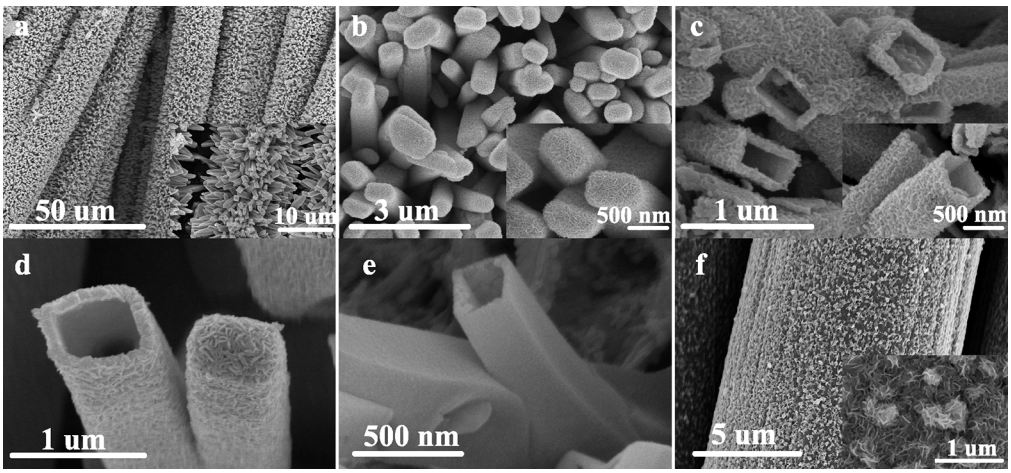

Figure 3. (a) SEM image of ZIF-67/CC. (b and c) High-magnification SEM images of CoS_2@MoS_2 nanorods/CC and HCMNTs/CC, respectively. (d)High-magnification SEM image of HCMNTs/CC etched for 1 h. (e and f) High-magnification SEM images of CoS_2 and MoS_2/CC, respectively.

and deposited by using it as a template. The nanotube structure is finally formed by etching, which greatly increases the reaction contact area and provides more active sites for the insertion of lithium ions. The core−shell hollow structure will effectively buffer the volume change that may occur during the storage reaction and inhibit the agglomeration of MoS_2. At the same time, the hollow structure can effectively shorten the electron path and improve the electrochemical performance of the electrode, forming a lithium battery storage material with excellent performance.[33,34] In order to realize the uniform coating of molybdenum sulfide and form a core−shell structure, it is very important to control the matching between the synthesis rate of MoS_2 and the vulcanization rate of CoS_2 in the hydrothermal reaction process. To clarify this, we estimate it by constructing the first-order reaction kinetic model and substituting it into the empirical formula of the reaction rate (Supporting Information for details).[35,36] The relative rate

$$R_{Co/Mo} = \frac{c_{Co}^{(l)}(r)/c_{Co}^{(0)}}{c_{Mo}^{(l)}(r)/c_{Mo}^{(0)}} \quad (1)$$

represents the relative generation rate of CoS_2 and MoS_2, where $c_{Co}^{(l)}(r)$ and $c_{Mo}^{(l)}(r)$ represent the local concentrations of CoS_2 and MoS_2, while $c_{Co}^{(0)}$ and $c_{Mo}^{(0)}$ represents the total concentration of them.[37] In Figure S1b, it can be clearly found that the value of $R_{Co/Mo}$ is close to 1, which indicates the rate matching between CoS_2 and MoS_2, revealing the stable ordering of the hierarchical structural construction. There is no obvious fluctuation in $R_{Co/Mo}$ as the reaction proceeds, which means that T = 473 K is the optimal choice for the formation of the CoS_2@MoS_2 core−shell structure.

The chemical states and structures of the samples were then investigated. Figure 2a shows the XRD patterns of the fabricated flexible electrodes. All displayed peak positions that match the standard diffraction peak positions of CoS_2 (JCPDS No. 41-7417) and are free of impurity peaks.[38] Among them, the obvious diffraction peaks at 32.3°, 36.2°, 39.8°, and 54.9° correspond to the (200), (210), (211), and (311) crystal planes of CoS_2, respectively, which proves the good crystallinity of the sample. The broad diffraction peaks between 20° and 30° belong to carbon cloth. The ultrathin few-layer structure results in no obvious MoS_2 characteristic peaks in the XRD results, but its existence can be confirmed in the Raman spectrum. The Raman spectrum shows two distinct characteristic peaks located at 378 and 402 cm^{-1}, which match the E_{2g}^1 and A_{1g} modes of MoS_2, respectively (illustration in Figure 2b.[39] The peak distance (Δk) between them is 24 cm^{-1}, indicating that the sample contains multilayered ultrathin MoS_2, which is also consistent with the XRD pattern.[40] Two distinct peaks can be observed at 1325 and 1600 cm^{-1}; the former corresponds to the D vibration band of carbon cloth, and the latter belongs to the G vibration band. The value of I_g/I_d is 1.05, indicating that the carbon cloth as the flexible electrode framework has good electrical conductivity.[41] The elemental composition of the prepared electrode was further analyzed by XPS. The results revealed that the nanotube array on the carbon cloth contained Co, O, Mo, S, and C elements (Figure 2c). The existence of the O element comes from the hydrophilic treatment when giving oxygen-containing functional groups on the surface of carbon cloth. Accordingly, the peaks of 161.8 and 162.9 eV in the S 2p high-resolution spectrum correspond to S $2p_{3/2}$ and S $2p_{1/2}$, respectively, symbolizing the S^{2-} valence state of the S element (Figure 2d).[42] In addition, the characteristic peaks at 232.3 and 229.1 eV in Figure 2f are deconvoluted as Mo $3d_{3/2}$ and Mo $3d_{5/2}$, respectively,[43,44] while the peak observed at 226.5 eV belongs to S 2s in MoS_2. At the same time, the spectrum of Co 2p can easily fit two characteristic peaks of 779.5 and 795.4 eV, corresponding to Co $2p_{3/2}$ and Co $2p_{1/2}$, respectively.[45] In addition, the two adjacent peaks at 785.1 and 801.4 eV are attributed to the existence of a Co−O bond, indicating that a Co−O−C bond is formed between the carbon cloth and the CoS_2 core, making the tubular CoS_2 firmly bonded to the substrate.[46,47] Furthermore, XPS test results show that the proportions of Co and Mo on the electrode surface are 5.56 and 16.36 atom %, respectively (Table S1). By inductively coupled plasma-optical emission spectroscopy (ICP-OES), it can be concluded that Co accounts for 3.86 wt % in the whole composite electrode, while the content of Mo is 1.29 wt %.

The blank carbon cloth fibers in Figure S2b are regularly arranged, the bare surface is smooth, and the diameter is 6−8 μm. In contrast, the surface of the product soaked in the prepared solution is purple (Figure S2a). As shown in Figure

https://doi.org/10.1021/acsaem.2c01675
ACS Appl. Energy Mater. 2022, 5, 10056−10066

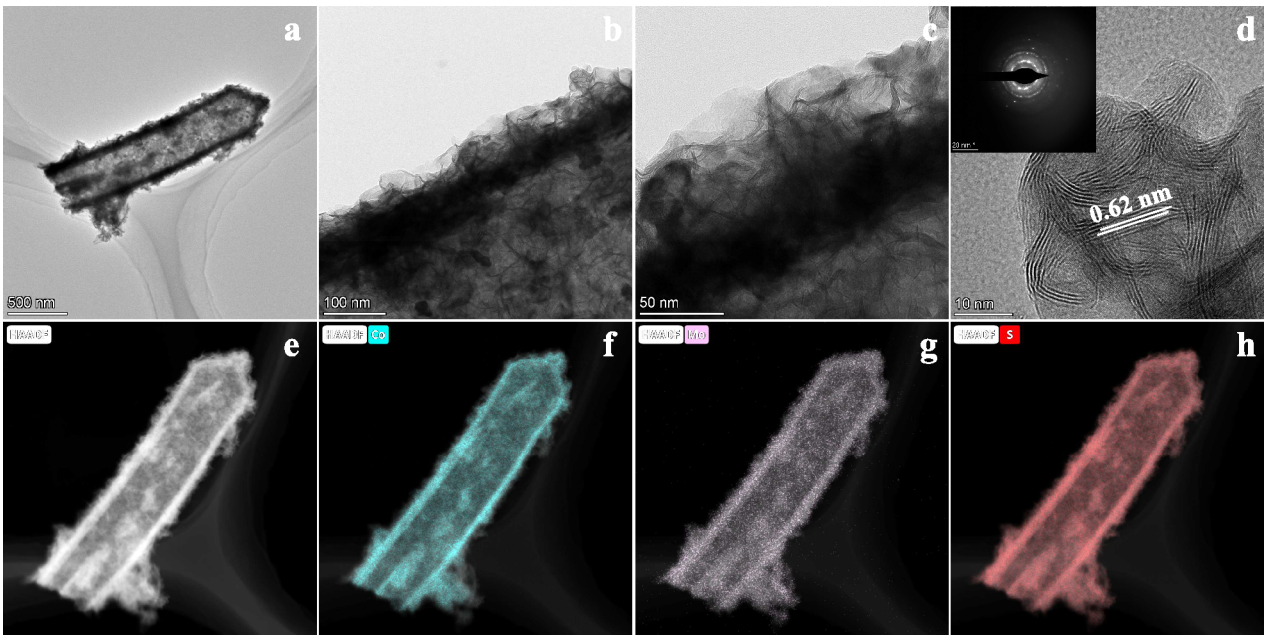

Figure 4. (a–c) TEM and (d) HRTEM images of CoS_2@MoS_2 nanotube. STEM image of CoS_2@MoS_2 nanotube and corresponding elemental mapping images of (e) HAADF, (f) Co, (g) Mo, and (h) S.

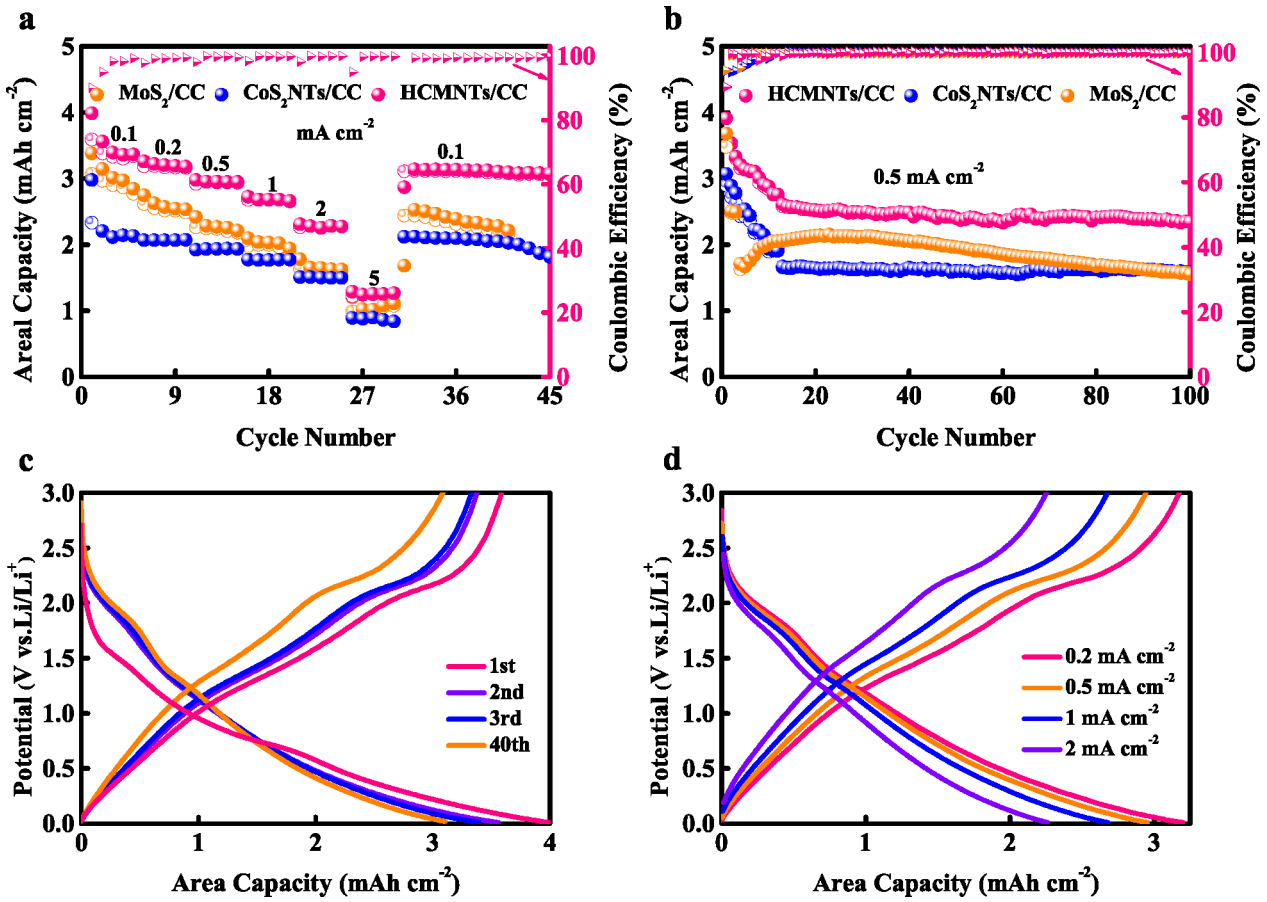

Figure 5. (a) Rate performance of the three composite electrodes at different current densities. (b) Cycling performance and Coulombic efficiency of the as-prepared electrodes cycled at 0.5 mA cm^{-2} for 100 cycles. GDC profiles of the HCMNTs/CC electrode (c) for the 1st, 2nd, 3rd, and 40th cycles at 0.1 mA cm^{-2} and (d) at increasing discharge current density from 0.2 to 2.0 mA cm^{-2}.

3a, ZIF-67 formed uniformly distributed nanorod arrays with diameters of 500–600 nm on the substrate, which served as the skeleton for subsequent reaction. After hydrothermal reaction, the staggered MoS_2 nanosheets were supported by tubular CoS_2 and still exhibited an array structure (Figure 3b). On the basis of retaining the one-dimensional topographical

https://doi.org/10.1021/acsaem.2c01675
ACS Appl. Energy Mater. 2022, 5, 10056–10066

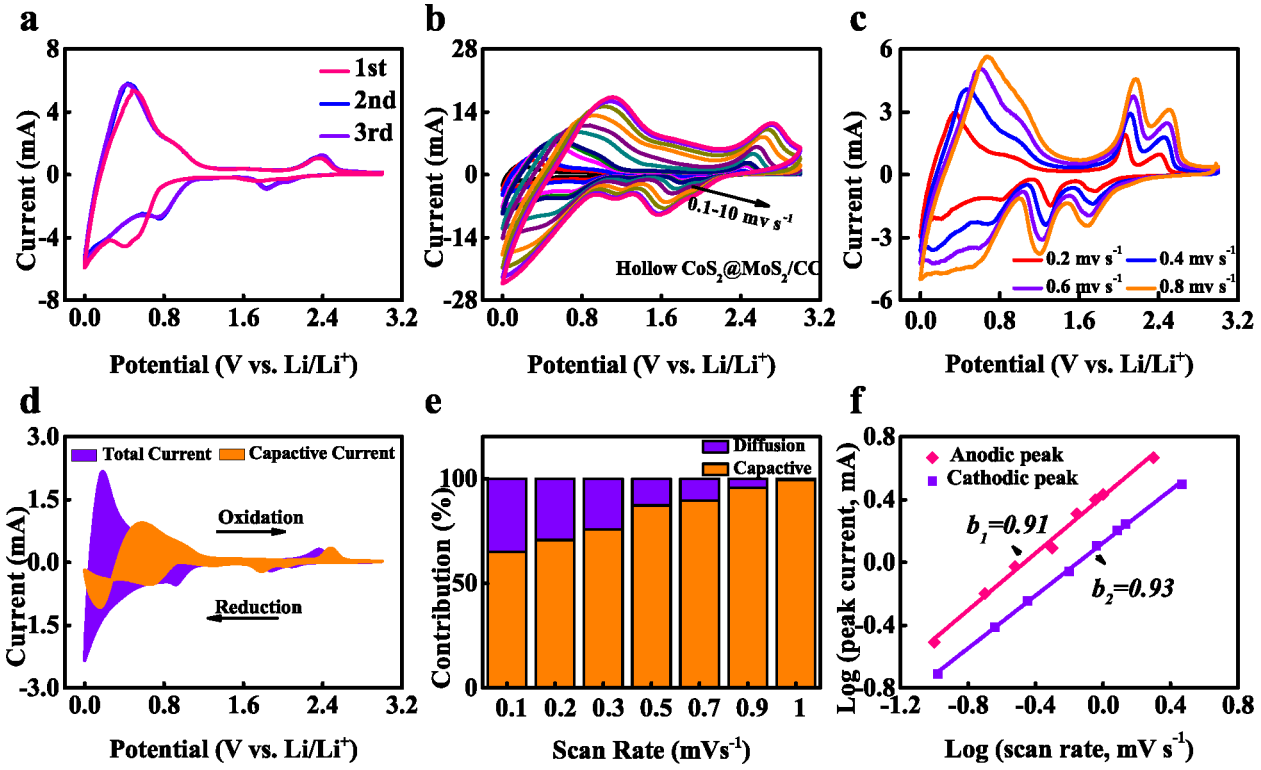

Figure 6. CV curves of the HCMNTs/CC electrode (a) at a scan rate of 0.5 mV/s and (b) at different rates from 0.1 to 10 mV/s in the range of 0.01−3.0 V vs Li/Li^+. (c) CV curves of the CoS_2 NTs/CC electrode at different rates from 0.2 to 0.8 mV/s. (d) Capacitive (orange) contribution of the HCMNTs/CC electrode at 0.1 mV/s. (e) Contribution of capacitance and diffusion-controlled process at different scan rates of 0.1−1 mV/s. (f) Graph of the logarithmic peak current and logarithmic scan rate of the HCMNTs/CC electrode.

properties, the surface of the nanorods becomes rough and the diameter increases to 600−700 nm. Compared with MoS_2 grown on bare carbon cloth (Figure 3f), the MOF provides a template for the in situ synthesis of MoS_2, avoiding its agglomeration. In addition, it can be clearly seen that there are a lot of voids between the MoS_2 nanosheets, which increases the reaction area for lithium-ion storage. The structure of the sample was then further constructed by adjusting the reaction time and TAA solution concentration (Figure 3d). However, excessive etching at high concentration will cause damage to the nanotube (Figure S2d). Similarly, hollow CoS_2 nanotube arrays with smooth surfaces can also be obtained by the same method (Figure 3e). The hollow CoS_2@MoS_2 nanotube was further observed in Figure 3c. The high-resolution SEM of the inset shows that the MoS_2 layer is uniformly attached and the hollow structure is evident after etching. Obviously, the hollow CoS_2 provides a skeleton for the growth of the MoS_2 shell with a certain thickness. The hierarchical structure of the hollow array was confirmed by TEM and HRTEM. Figure 4a shows that the CoS_2@MoS_2 array is a distinct hollow nanotube with a diameter of around 600 nm, which is corroborated by the SEM images. It can be observed from Figure 4b and 4c that the MoS_2 shell is uniformly attached to the outside of the hollow CoS_2 core with obvious delamination. A lattice spacing of 0.62 nm in the outer layer spacing was observed to correspond to the (002) crystal plane of MoS_2 (Figure 4d). Meanwhile, the mapping distribution of EDS elements is presented in Figure 4e−h, indicating that the Co, Mo, and S elements are uniformly distributed throughout the structure. The position of Mo indicates that MoS_2 is also attached to the inner walls of the nanotubes. The overall distribution confirms the tight binding of CoS_2 and MoS_2, which ensures the stability of the structure. This hollow core−shell structure simultaneously increases the reaction area and provides stable electrochemical performance.

We assembled the 2032-type coin half-cell with the prepared flexible electrodes to study its excellent electrochemical performance. Obviously, HCMNTs/CC has the best rate capability at different current densities among all samples. Reversible areal specific capacities of 3.36, 3.18, 2.95, 2.67, 2.28, and 1.27 mAh cm^{-2} were obtained at current densities of 0.1, 0.2, 0.5, 1, 2, and 5 mA cm^{-2}, respectively (Figure 5a). At the same time, it exhibits stronger stability compared with other samples, which also confirms its excellent structure. After 5 cycles at a high density of 5 mA cm^{-2}, the areal specific capacity of 3.12 mAh cm^{-2} was restored immediately, showing outstanding reversibility. For comparison, the MoS_2/CC (MCC) and CoS_2/CC electrodes were also measured. The rate performance of them is relatively poor, and the specific capacities are only 1.08 and 0.84 mAh cm^{-2}, respectively, at 5 mA cm^{-2}. Moreover, they were only restored to 2.16 and 2.03 mAh cm^{-2} at 0.1 mA cm^{-2} after 30 cycles. The long-term cycling performance is shown in Figure 5b, and the capacity is still as high as 2.35 mAh cm^{-2} after 100 cycles at 0.5 mA cm^{-2} with an initial Coulombic efficiency of 89.4% (the Coulombic efficiency reaches 99.9%). This is attributed to its unique structure that effectively facilitates the penetration of electrolytes and the charge transfer of ions. The CoS_2 NTs/CC electrode maintains a relatively stable cycle performance due to its nanotube structure, but it only reaches 1.58 mAh cm^{-2} after 100 cycles (Coulomb efficiency reaches 99.9%). In contrast, the capacity of the MoS_2/CC electrode shows a decreasing

https://doi.org/10.1021/acsaem.2c01675
ACS Appl. Energy Mater. 2022, 5, 10056−10066

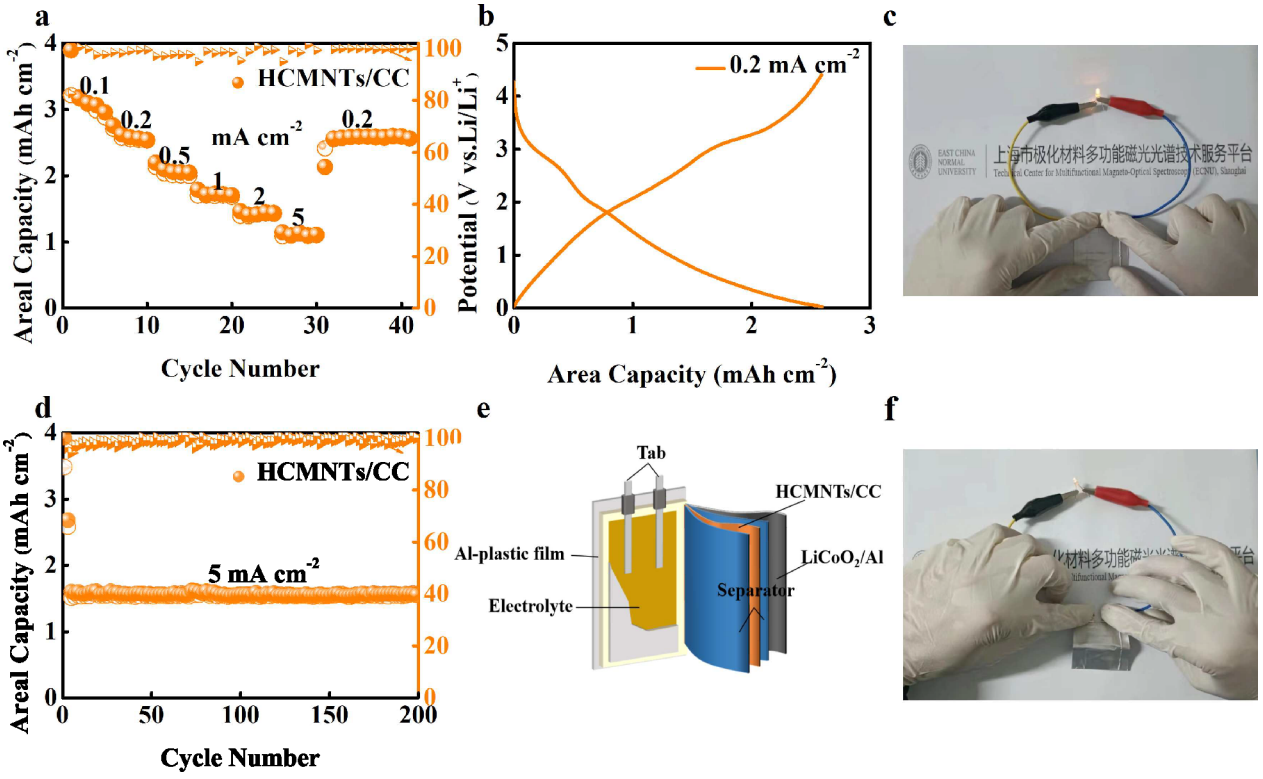

Figure 7. (a) Rate performance of the coin-type full cell at different current densities. (b) GDC profile of the coin-type full cell at 0.2 mA cm^{-2}. Demonstration of an LED light by the soft pack battery in the (c) unfolded state and (f) after bending for 200 times. (d) Cycling performance and Coulombic efficiency of the full cell cycled at 5 mA cm^{-2} for 200 cycles. (e) Schematic diagram of the soft pack battery.

trend, which is due to the agglomeration and accumulation of MoS_2 during cycling, resulting in the capacity loss. To better explore the morphology after electrochemical reaction, we performed SEM analysis of the electrode after cycling. After washing with dimethyl carbonate solvent, the morphologies of the samples after 100 cycles are shown in Figure S3a and S3b. It can be seen that the CoS_2@MoS_2 nanotubes are still well maintained, and the integrity of the electrode is preserved. It is proved that the intact core−shell structure can effectively reduce the volume expansion and ensure the orderly progress of the lithium storage reaction, which is consistent with the robust cycling performance of HCMNTs/CC electrodes.

Figure 5c demonstrates the galvanostatic discharge/charge (GDC) process of the HCMNTs/CC electrode in the voltage range of 0.01−3.0 V (0.1 mA cm^{-2}). There are two distinct discharge plateaus at ∼1.5 and ∼0.7 V in the first cycle. In subsequent cycles, the discharge plateau of 1.9 V and the charge plateau of 2.3 V symbolize the conversion reaction between S and Li_2S. It is noted that the capacity drop is accompanied by a shift in the platform position, implying the emergence of a solid electrolyte interface (SEI) film during the reaction. The subsequent reaction maintains the same voltage position (the 30th cycle), which reflects the stability of the electrode cycle. The GDC curves at different current densities are shown in Figure 5d (0.2−2 mA cm^{-2}). It can be seen that when the current density changes, the position of a similar platform still tends to be stable. The increase of current density is accompanied by the decrease of capacity caused by the polarization process, but the capacity is still as high as 2.26 mAh cm^{-2} at 2 mA cm^{-2}, which proves that HCMNTs/CC as an electrode has strong lithium-ion transmission capacity and stable structural characteristics.

The first three cyclic voltammogram (CV) curves of HCMNTs/CC at 0.5 mV s^{-2} are shown in Figure 6a (voltage window of 0.01−3 V). During the first cycle of discharge, distinct peaks can be observed at ∼1.75 and ∼0.4 V. This may correspond to the insertion of Li ions into the MoS_2 layer to form Li_xMoS_2 and the further reaction of Li_xMoS_2 with Li ions to convert Li_2S and Mo, respectively.[48] The process is accompanied by the formation of irreversible SEI films, resulting in unavoidable capacity loss.[49] The peak at ∼2.35 V during charging is attributed to the oxidation of Li_2S to Li^+ and S. The subsequent two discharge cycles showed a new peak at ∼1.8 V, corresponding to the reduction of S to Li_2S. Other peaks are determined by CoS_2 and CC substrate, and the voltage values basically coincide (Figure 6c, Figure S4a and S4b), symbolizing the stable electrochemical performance of the electrode material. To further clarify the structural advantages of HCMNTs/CC, we investigated its ion diffusion kinetics through CV curves at different scan rates (Figure 6b). It is evident that the peak intensity of the current increases with the scan rate. From previous reports, there is a power exponential relationship between the current intensity (i) and the scanning rate (v): $i = av^b$.[50,51] Generally, when the value of b is close to 0.5, the dominant process of lithium dissociation storage is diffusion behavior, while when the value of b is close to 1, the capacitance effect is dominant. By calculating the slopes of log(i) and log(v), the b values of the cathode peak and anode peak are 0.93 and 0.91, respectively (Figure 6f), indicating that the charge storage dynamics of the electrode is mainly provided for the capacitance behavior.[52] The proportion of capacitive contribution can be quantitatively analyzed by calculating the Dunn equation as follows: $i = k_1\nu^{1/2} + k_2\nu$.[53,54] Figure 6d shows that the capacitance effect

https://doi.org/10.1021/acsaem.2c01675
ACS Appl. Energy Mater. 2022, 5, 10056−10066

contribution is 64.92% (orange area) at a scan rate of 0.1 mV/s. The capacitance behavior ratio gradually increased with increasing scanning rate and finally reached 99% at 1 mV/s (Figure 6e, Figure S4d). The results show that the hollow nanotube structure of the HCMNTs/CC electrode provides a high pseudocapacitance effect and ensures high stable lithium-ion storage.

The electrochemical impedance spectrum (EIS) was further studied (Figure S5a). Compared with other electrodes, HCMNTs/CC has the smallest semicircle in the medium- and high-frequency region of the Nyquist diagram, implying the lowest SEI layer charge diffusion resistance (R_f) and electrode/electrolyte interface charge transfer resistance (R_{ct}).[55] Then, the parameters extracted by the fitting circuit are used to quantitatively analyze the impedance (Figure S5b). It can be seen from Figure S5d that the initial R_{ct} of HCMNTs/CC is only 40.98 Ω compared with the MoS_2/CC (44.12 Ω) and CoS_2 NTs/CC (59.29 Ω) electrodes. With the activation of the electrode material, the R_{ct} decreased to 25.22 Ω after 50 cycles and reached 20.96 Ω after 100 cycles, indicating that the electrode has efficient charge transport capability. In addition, the linear part of the low-frequency region represents the Warburg impedance (W), which is related to the diffusion of lithium ions. The low-frequency resistance has the following linear relationship with $\omega^{-1/2}$ $Z' = K + \sigma\omega^{-1/2}$, where K is a constant and ω corresponds to the frequency, so the Warburg coefficient σ in different cycle stages can be obtained from the curve in Figure S5c.[56] The lithium-ion diffusion coefficient can be further confirmed by the specific equation

$$D = \frac{R^2T^2}{2A^2n^4F^4C^2\sigma^2} \quad (2)$$

where R is the gas constant (8.314 J mol^{-1} K^{-1}), T is the absolute temperature (298.15 K), and F is the Faraday constant (96 486 C mol^{-1}). In addition, A, n, and C are the number of charge transfers during the reaction, the total area of the reaction electrode (cm^2), and the molar concentration of lithium ions (mol cm^{-3}), respectively.[57] The calculation shows that the initial Li-ion diffusion coefficient of the HCMNTs/CC electrode is 1.78×10^{-12} cm^2/s, which is higher than that of the MCC electrode (1.69×10^{-12} cm^2/s) and CoS_2 NTs/CC electrode (0.57×10^{-12} cm^2/s), and reaches 0.31×10^{-10} cm^2/s after 100 cycles. This result further shows that the unique structure of HCMNTs/CC enhances the lithium storage kinetics and promotes the diffusion of lithium ions. The array morphology of HCMNTs increases the effective contact area of the reaction. At the same time, the synergy between the structures shortens the diffusion path of the ions, reduces the charge transfer resistance, and finally achieves strong cycle performance.

To demonstrate the anode performance of HCMNTs/CC, HCMNTs/CC//$LiCoO_2$/Al coin-type full cells were further assembled for testing. The voltage window for rate and cycling tests of the cells is 1.0−4.2 V. It can be observed that the device still maintains good rate performance between 0.1 and 5 mA cm^{-2}, and the capacity remains at 2.55 mAh cm^{-2} when recovered to 0.2 mA cm^{-2} (Figure 7a). Correspondingly, a clear charge−discharge plateau can still be observed in the GDC curve of Figure 7b, proving that the full cell has a stable redox reaction process. Even in the long-cycle test at 5 mA cm^{-2}, the Coulombic efficiency of the first cycle still reached 88.7% and the area specific capacity was stable around 1.55 mAh cm^{-2} after 200 cycles (Figure 7d). On the basis of its outstanding rate capability and cycling stability, the flexible LIB full cell shown in Figure 7e was assembled. Whether in the stretched state (Figure 7c) or the state after being folded many times (Figure 7f), it was observed that the pouch battery could still ensure stable capacity output and light up the yellow LED (3 V, 0.2 W). In addition, even if the electrode has been folded many times, the LED can still maintain normal operation during the dynamic folding process, proving excellent flexibility and stability (Video S1, Supporting Information).

4. CONCLUSIONS

In conclusion, we demonstrate that hierarchical MoS_2 nanotubes supported by tubular CoS_2 on carbon cloth are used as flexible Li-ion electrodes. In the process of precursor synthesis and etching, the density and hollow structure of the nanoarrays are controlled by the reaction conditions. This structure ensures sufficient contact between the active material and the electrolyte, providing an outstanding high areal specific capacity. In the half-cell test, a high areal specific capacity of 2.35 mAh cm^{-2} was retained after 100 cycles at 0.5 mA cm^{-2}. At the same time, the hollow core−shell structure alleviates the volume change and effectively inhibits the agglomeration of MoS_2, ensuring the stability and order of the reaction process. Furthermore, the assembled flexible full cells exhibit excellent stretchability, providing stable capacity output. This work provides a new idea for the application of wearable flexible devices.

■ ASSOCIATED CONTENT

Supporting Information

The Supporting Information is available free of charge at https://pubs.acs.org/doi/10.1021/acsaem.2c01675.

Dependence of $k_{Co/Mo}$ on reaction temperature and relationship between $R_{Co/Mo}$ and reaction degree; SEM images of bare CC, ZIF-67/CC reacted for 4 h, sample etched with high concentration TAA; SEM images of HCMNTs/CC anode after 100 cycles; CV curves of CC and CoS_2 NTs/CC electrode at different rates in the range of 0.01−3.0 V vs Li/Li$^+$; capacitive contribution of HCMNTs/CC electrode at 1 mV/s; electrochemical impedance spectra of each electrode at different cycles; equivalent circuit used in electrochemical impedance spectroscopy; relationship plots between Z and $\omega^{-1/2}$ in the low-frequency range of HCMNTs/CC at different cycles; schematic diagram of the R_{ct} value of each electrode and HCMNTs/CC at different cycles; atomic percentages generated by XPS analysis (PDF)

Video showing the LED maintaining normal operation during the dynamic folding process (MP4)

■ AUTHOR INFORMATION

Corresponding Authors

Liangqing Zhu − *Technical Center for Multifunctional Magneto-Optical Spectroscopy (Shanghai), Department of Physics, School of Physics and Electronic Science, East China Normal University, Shanghai 200241, China;* Email: lqzhu@ee.ecnu.edu.cn

Zhigao Hu − *Technical Center for Multifunctional Magneto-Optical Spectroscopy (Shanghai), Department of Physics, School of Physics and Electronic Science, East China Normal University, Shanghai 200241, China; Collaborative*

https://doi.org/10.1021/acsaem.2c01675
ACS Appl. Energy Mater. 2022, 5, 10056−10066

Innovation Center of Extreme Optics, Shanxi University, Taiyuan, Shanxi 030006, China; orcid.org/0000-0003-0575-2191; Email: zghu@ee.ecnu.edu.cn

Authors

Shenyu Du − *Technical Center for Multifunctional Magneto-Optical Spectroscopy (Shanghai), Department of Physics, School of Physics and Electronic Science, East China Normal University, Shanghai 200241, China*

Liyuan Ao − *Technical Center for Multifunctional Magneto-Optical Spectroscopy (Shanghai), Department of Physics, School of Physics and Electronic Science, East China Normal University, Shanghai 200241, China;* orcid.org/0000-0001-6179-3639

Jianli Tang − *Technical Center for Multifunctional Magneto-Optical Spectroscopy (Shanghai), Department of Physics, School of Physics and Electronic Science, East China Normal University, Shanghai 200241, China*

Kai Jiang − *Technical Center for Multifunctional Magneto-Optical Spectroscopy (Shanghai), Department of Physics, School of Physics and Electronic Science, East China Normal University, Shanghai 200241, China*

Liyan Shang − *Technical Center for Multifunctional Magneto-Optical Spectroscopy (Shanghai), Department of Physics, School of Physics and Electronic Science, East China Normal University, Shanghai 200241, China;* orcid.org/0000-0003-2341-3978

Yawei Li − *Technical Center for Multifunctional Magneto-Optical Spectroscopy (Shanghai), Department of Physics, School of Physics and Electronic Science, East China Normal University, Shanghai 200241, China;* orcid.org/0000-0001-8776-5687

Jinzhong Zhang − *Technical Center for Multifunctional Magneto-Optical Spectroscopy (Shanghai), Department of Physics, School of Physics and Electronic Science, East China Normal University, Shanghai 200241, China;* orcid.org/0000-0003-1511-4281

Junhao Chu − *Technical Center for Multifunctional Magneto-Optical Spectroscopy (Shanghai), Department of Physics, School of Physics and Electronic Science, East China Normal University, Shanghai 200241, China; Collaborative Innovation Center of Extreme Optics, Shanxi University, Taiyuan, Shanxi 030006, China*

Complete contact information is available at: https://pubs.acs.org/10.1021/acsaem.2c01675

Notes

The authors declare no competing financial interest.

■ ACKNOWLEDGMENTS

This work was financially supported by the National Natural Science Foundation of China (Grant Nos. 62090013, 61974043, and 62074058), the National Key R&D Program of China (Grant No. 2019YFB2203403), the Projects of Science and Technology Commission of Shanghai Municipality (Grant Nos. 21JC1402100 and 19511120100), and the Program for Professor of Special Appointment (Eastern Scholar) at Shanghai Institutions of Higher Learning and Shanghai Pujiang Program (20PJ1403600).

■ REFERENCES

(1) Zhang, L. P.; Li, X. L.; Yang, M. R.; Chen, W. H. High-safety separators for lithium-ion batteries and sodium-ion batteries: advances and perspective. *Energy Stor. Mater.* **2021**, *41*, 522−545.
(2) Kim, T.; Song, W. T.; Son, D. Y.; Ono, L. K.; Qi, Y. B. Lithium-ion batteries: outlook on present, future, and hybridized technologies. *J. Mater. Chem. A* **2019**, *7*, 2942.
(3) Chayambuka, K.; Mulder, G.; Danilov, D. L.; Notten, P. H. L. From Li-Ion Batteries toward Na-Ion Chemistries: Challenges and Opportunities. *Adv. Energy Mater.* **2020**, *10*, 2001310.
(4) Neumann, J.; Petranikova, M.; Meeus, M.; Gamarra, J. D.; Younesi, R.; Winter, M.; Nowak, S. Recycling of Lithium-Ion Batteries-Current State of the Art, Circular Economy, and Next Generation Recycling. *Adv. Energy Mater.* **2022**, *12*, 2102917.
(5) Zhai, Q. F.; Xiang, F. W.; Cheng, F.; Sun, Y. J.; Yang, X. P.; Lu, W.; Dai, L. M. Recent advances in flexible/stretchable batteries and integrated devices. *Energy Stor. Mater.* **2020**, *33*, 116−138.
(6) Li, H. F.; Tang, Z. J.; Liu, Z. X.; Zhi, C. Y. Evaluating Flexibility and Wearability of Flexible Energy Storage Devices. *Joule* **2019**, *3*, 613−619.
(7) Fu, K. K.; Cheng, J.; Li, T.; Hu, L. B. Flexible Batteries: From Mechanics to Devices. *ACS Energy Lett.* **2016**, *1*, 1065−1079.
(8) Wu, Z. P.; Wang, Y. L.; Liu, X. B.; Lv, C.; Li, Y. S.; Wei, D.; Liu, Z. F. Carbon-Nanomaterial-Based Flexible Batteries for Wearable Electronics. *Adv. Mater.* **2019**, *31*, 1800716.
(9) Fang, Z. H.; Wang, J.; Wu, H. C.; Li, Q. Q.; Fan, S. H.; Wang, J. P. Progress and challenges of flexible lithium ion batteries. *J. Power Sources* **2020**, *454*, 227932.
(10) Wang, X. H.; Guan, C.; Sun, L. M.; Susantyoko, R. A.; Fan, H. J.; Zhang, Q. Highly stable and flexible Li-ion battery anodes based on TiO_2 coated 3D carbon nanostructures†. *J. Mater. Chem. A* **2015**, *3*, 15394.
(11) Tao, T.; Lu, S. G.; Chen, Y. A Review of Advanced Flexible Lithium-Ion Batteries. *Adv. Mater. Technol.* **2018**, *3*, 1700375.
(12) Liu, B.; Zhang, J.; Wang, X. F.; Chen, G.; Chen, D.; Zhou, C. W.; Shen, G. Z. Hierarchical Three-Dimensional $ZnCo_2O_4$ Nanowire Arrays/Carbon Cloth Anodes for a Novel Class of High-Performance Flexible Lithium-Ion Batteries. *Nano Lett.* **2012**, *12*, 3005−3011.
(13) Weng, W.; Lin, H. J.; Chen, X. L.; Ren, J.; Zhang, Z. T.; Qiu, L. B.; Guan, G. Z.; Peng, H. S. Flexible and stable lithium ion batteries based on three-dimensional aligned carbon nanotube/silicon hybrid electrodes†. *J. Mater. Chem. A* **2014**, *2*, 9306.
(14) Pan, Z.; Ren, J.; Guan, G.; Fang, X.; Wang, B.; Doo, S.-G.; Son, I. H.; Huang, X.; Peng, H. Synthesizing Nitrogen-Doped Core-Sheath Carbon Nanotube Films for Flexible Lithium Ion Batteries. *Adv. Energy Mater.* **2016**, *6*, 1600271.
(15) Yehezkel, S.; Auinat, M.; Sezin, N.; Starosvetsky, D.; Ein-Eli, Y. Bundled and densified carbon nanotubes (CNT) fabrics as flexible ultra-light weight Li-ion battery anode current collectors. *J. Power Sources* **2016**, *312*, 109−115.
(16) Guan, C.; Wang, X. H.; Zhang, Q.; Fan, Z. X.; Zhang, H.; Fan, H. J. Highly Stable and Reversible Lithium Storage in SnO_2 Nanowires Surface Coated with a Uniform Hollow Shell by Atomic Layer Deposition. *Nano Lett.* **2014**, *14*, 4852−4858.
(17) Luo, B.; Hu, Y. X.; Zhu, X. B.; Qiu, T. F.; Zhi, L. J.; Xiao, M.; Zhang, H. J.; Zou, M. C.; Cao, A. Y.; Wang, L. Z. Controllable growth of SnS_2 nanostructures on nanocarbon surfaces for lithium-ion and sodium-ion storage with high rate capability†. *J. Mater. Chem. A* **2018**, *6*, 1462−1472.
(18) Yang, Q.; Wang, Y. K.; Li, X. L.; Li, H. F.; Wang, Z. F.; Tang, Z. J.; Ma, L. T.; Mo, F. N.; Zhi, C. Y. Recent Progress of MXene-Based Nanomaterials in Flexible Energy Storage and Electronic Devices. *Energy Environ. Mater.* **2018**, *1*, 183−195.
(19) Huang, Y. C.; Yang, H.; Xiong, T. Z.; Adekoya, D.; Qiu, W. T.; Wang, Z. M.; Zhang, S. Q.; Balogun (J. Tang), M. S. Adsorption energy engineering of nickel oxide hybrid nanosheets for high areal capacity flexible lithium-ion batteries. *Energy Storage Mater.* **2020**, *25*, 41−51.

(20) Huang, Y. C.; Guo, Z. J.; Liu, H.; Zhang, S. Q.; Wang, P. S.; Lu, J.; Tong, Y. X. Heterojunction Architecture of N-Doped WO_3 Nanobundles with Ce_2S_3 Nanodots Hybridized on a Carbon Textile Enables a Highly Efficient Flexible Photocatalyst. *Adv. Funct. Mater.* **2019**, *29*, 1903490.
(21) Cao, X. H.; Tan, C. L.; Zhang, X.; Zhao, W.; Zhang, H. Solution-Processed Two-Dimensional Metal Dichalcogenide-Based Nanomaterials for Energy Storage and Conversion. *Adv. Mater.* **2016**, *28*, 6167−6196.
(22) Mendoza-Sanchez, B.; Gogotsi, Y. Synthesis of Two-Dimensional Materials for Capacitive Energy Storage. *Adv. Mater.* **2016**, *28*, 6104−6135.
(23) Cui, L. F.; Hu, L. B.; Choi, J. W.; Cui, Y. Light-Weight Free-Standing Carbon Nanotube-Silicon Films for Anodes of Lithium Ion Batterie. *ACS Nano* **2010**, *4* (7), 3671−3678.
(24) Hu, L.; Wu, H.; La Mantia, F.; Yang, Y.; Cui, Y. Thin, Flexible Secondary Li-Ion Paper Batteries. *ACS Nano* **2010**, *4* (10), 5843−5848.
(25) Yu, H. L.; Zhu, C. L.; Zhang, K.; Chen, Y. J.; Li, C. Y.; Gao, P.; Yang, P. P.; Ouyang, Q. Y. *J. Mater. Chem. A* **2014**, *2*, 4551−4557.
(26) Deng, Z. N.; Jiang, H.; Hu, Y. J.; Liu, Y.; Zhang, L.; Liu, H. L.; Li, C. Z. 3D Ordered Macroporous MoS_2@C Nanostructure for Flexible Li-Ion Batteries. *Adv. Mater.* **2017**, *29*, 1603020.
(27) Du, S. Y.; Wu, C.; Ao, L. Y.; Zhou, X.; Jiang, K.; Shang, L. Y.; Li, Y. W.; Zhang, J. Z.; Hu, Z. G.; Chu, J. H. Significantly enhanced lithium storage by in situ grown CoS_2@MoS_2 core-shell nanorods anchored on carbon cloth. *Chem. Eng. J.* **2021**, *420*, 127714.
(28) Wang, C.; Wan, W.; Huang, Y. H.; Chen, J. T.; Zhou, H. H.; Zhang, X. X. Hierarchical MoS_2 nanosheet/active carbon fiber cloth as a binder-free and free-standing anode for lithium-ion batteries†. *Nanoscale* **2014**, *6*, 5351−5358.
(29) Yu, D. B.; Ge, L.; Wu, B.; Wu, L.; Wang, H. T.; Xu, T. W. Precisely tailoring ZIF-67 nanostructures from cobalt carbonate hydroxide nanowire arrays: toward high-performance battery-type electrodes†. *J. Mater. Chem. A* **2015**, *3*, 16688−16694.
(30) Bose, R.; Jin, Z. Y.; Shin, S.; Kim, S.; Lee, S. Y.; Min, Y. S. Co-catalytic Effects of CoS_2 on the Activity of the MoS_2 Catalyst for Electrochemical Hydrogen Evolution. *Langmuir* **2017**, *33*, 5628−5635.
(31) Wang, Y. W.; Yu, L.; Lou, X. W. Synthesis of Highly Uniform Molybdenum-Glycerate Spheres and Their Conversion into Hierarchical MoS_2 Hollow Nanospheres for Lithium-Ion Batteries. *Angew. Chem., Int. Ed.* **2016**, *55*, 7423−7426.
(32) Yu, X. Y.; Yu, L.; Lou, X. W. Hollow Nanostructures of Molybdenum Sulfides for Electrochemical Energy Storage and Conversion. *Small Methods* **2017**, *1*, 1600020.
(33) Wang, Y.; Qu, Q. T.; Li, G. C.; Gao, T.; Qian, F.; Shao, J.; Liu, W. J.; Shi, Q.; Zheng, H. H. 3D Interconnected and Multiwalled Carbon@MoS_2@Carbon Hollow Nanocables as Outstanding Anodes for Na-Ion Batteries. *Small* **2016**, *12* (43), 6033−6041.
(34) Tang, W. J.; Wang, X. L.; Xie, D.; Xia, X. H.; Gu, C. D.; Tu, J. P. Hollow metallic 1T MoS_2 arrays grown on carbon cloth: a freestanding electrode for sodium ion batteries†. *J. Mater. Chem. A* **2018**, *6*, 18318−18324.
(35) Zhu, C.; Mu, X.; van Aken, P. A.; Maier, J.; Yu, Y. Single-Layered Ultrasmall Nanoplates of MoS_2 Embedded in Carbon Nanofibers with Excellent Electrochemical Performance for Lithium and Sodium Storage. *Adv. Energy Mater.* **2015**, *5*, 1401170.
(36) Sun, X. R.; Zhang, H. W.; Zhou, L.; Huang, X. D.; Yu, C. Z. Polypyrrole-Coated Zinc Ferrite Hollow Spheres with Improved Cycling Stability for Lithium-Ion Batteries. *Small* **2016**, *12*, 3732−3737.
(37) Sun, Y. G.; Alimohammadi, F.; Zhang, D. T.; Guo, G. S. Enabling Colloidal Synthesis of Edge-Oriented MoS_2 with Expanded Interlayer Spacing for Enhanced HER Catalysis. *Nano Lett.* **2017**, *17*, 1963−1969.
(38) Jin, R. C.; Yang, L. X.; Li, G. H.; Chen, G. Hierarchical worm-like CoS_2 composed of ultrathin nanosheets as an anode material for lithium-ion batteries†. *J. Mater. Chem. A* **2015**, *3*, 10677−10680.
(39) Lee, Y. H.; Zhang, X. Q.; Zhang, W. J.; Chang, M. T.; Lin, C. T.; Chang, K. D.; Yu, Y. C.; Wang, J. T. W.; Chang, C. S.; Li, L. J.; Lin, T. W. Synthesis of Large-Area MoS_2 Atomic Layers with Chemical Vapor Deposition. *Adv. Mater.* **2012**, *24*, 2320−2325.
(40) Yu, Y. F.; Li, C.; Liu, Y.; Su, L. Q.; Zhang, Y.; Cao, L. Y. High-Quality Monolayer and Few-layer MoS_2 Films. *Sci. Rep.* **2013**, *3*, 1866.
(41) Wang, C.; Wan, W.; Huang, Y. H.; Chen, J. T.; Zhou, H. H.; Zhang, X. X. Hierarchical MoS_2 nanosheet/active carbon fiber cloth as a binder-free and free-standing anode for lithium-ion batteries†. *Nanoscale* **2014**, *6*, 5351−5358.
(42) Fan, X. B.; Xu, P. T.; Zhou, D. K.; Sun, Y. F.; Li, Y. G. C.; Nguyen, M. A. T.; Terrones, M.; Mallouk, T. E. Fast and Efficient Preparation of Exfoliated 2H MoS_2 Nanosheets by Sonication-Assisted Lithium Intercalation and Infrared Laser-Induced 1T to 2H Phase Reversion. *Nano Lett.* **2015**, *15* (9), 5956−5960.
(43) Wang, P. P.; Sun, H. Y.; Ji, Y. J.; Li, W. H.; Wang, X. Three-Dimensional Assembly of Single-Layered MoS_2. *Adv. Mater.* **2014**, *26*, 964−969.
(44) Chen, Y. M.; Yu, X. Y.; Li, Z.; Paik, U.; Lou, X. W. Hierarchical MoS_2 tubular structures internally wired by carbon nanotubes as a highly stable anode material for lithium-ion batteries. *Sci. Adv.* **2016**, *2*, No. e1600021.
(45) Huang, Q.; Wei, T.; Zhang, M.; Dong, L. Z.; Zhang, A. M.; Li, S. L.; Liu, W. J.; Liu, J.; Lan, Y. Q. A highly stable polyoxometalate-based metal-organic framework with π-π stacking for enhancing lithium ion battery performance†. *J. Mater. Chem. A* **2017**, *5*, 8477−8483.
(46) Ouyang, C. B.; Feng, S.; Huo, J.; Wang, S. Y. Three-dimensional hierarchical MoS_2 /CoS_2 heterostructure arrays for highly efficient electrocatalytic hydrogen evolution. *Green Energy Environ* **2017**, *2*, 134−141.
(47) Ouyang, C. B.; Wang, X.; Wang, S. Y. Phosphorus-doped CoS_2 nanosheet arrays as ultra-efficient electrocatalysts for the hydrogen evolution reaction†. *Chem. Commun.* **2015**, *51*, 14160−14163.
(48) Zhang, L.; Sun, D.; Kang, J.; Feng, J.; Bechtel, H. A.; Wang, L. W.; Cairns, E. J.; Guo, J. H. Electrochemical Reaction Mechanism of the MoS_2 Electrode in a Lithium-Ion Cell Revealed by in Situ and Operando X-ray Absorption Spectroscopy. *Nano Lett.* **2018**, *18*, 1466−1475.
(49) Ao, L. Y.; Wu, C.; Xu, Y. N.; Wang, X.; Jiang, K.; Shang, L. Y.; Li, Y. W.; Zhang, J. Z.; Hu, Z. G.; Chu, J. H. A novel Sn particles coated composite of SnO_x/ZnO and N-doped carbon nanofibers as high-capacity and cycle-stable anode for lithium-ion batteries. *J. Alloys Compd.* **2020**, *819*, 153036.
(50) Wu, C.; Xu, Y. N.; Ao, L. Y.; Jiang, K.; Shang, L. Y.; Li, Y. W.; Hu, Z. G.; Chu, J. H. Robust three-dimensional porous rGO aerogel anchored with ultra-fine a-Fe_2O_3 nanoparticles exhibit dominated pseudocapacitance behavior for superior lithium storage. *J. Alloys Compd.* **2020**, *816*, 152627.
(51) Lim, E.; Shim, H.; Fleischmann, S.; Presser, V. Fast and stable lithium-ion storage kinetics of anatase titanium dioxide/carbon onion hybrid electrodes†. *J. Mater. Chem. A* **2018**, *6*, 9480−9488.
(52) Gao, S. H.; Shi, G. S.; Fang, H. P. Impact of cation-π interactions on the cell voltage of carbon nanotube-based Li batteries†. *Nanoscale* **2016**, *8*, 1451−1455.
(53) Ao, L. Y.; Wu, C.; Wang, X.; Xu, Y. N.; Jiang, K.; Shang, L. Y.; Li, Y. W.; Zhang, J. Z.; Hu, Z. G.; Chu, J. H. Superior and Reversible Lithium Storage of SnO_2/Graphene Composites by Silicon Doping and Carbon Sealing. *ACS Appl. Mater. Interfaces* **2020**, *12*, 20824−20837.
(54) Chen, C. M.; Yang, Y. C.; Ding, S. S.; Wei, Z. X.; Tang, X.; Li, P. C.; Wang, T. H.; Cao, G. Z.; Zhang, M. S-doped carbon@TiO_2 to store Li^+/Na^+ with high capacity and long life-time. *Energy Stor. Mater.* **2018**, *13*, 215−222.
(55) Xu, Z. W.; Wang, T.; Kong, L.; Yao, K.; Fu, H.; Li, K.; Cao, L. Y.; Huang, J. F.; Zhang, Q. L. MoO_2@MoS_2 Nanoarchitectures for High-Loading Advanced Lithium-Ion Battery Anodes. *Part. Part. Syst. Charact* **2017**, *34*, 1600223.

https://doi.org/10.1021/acsaem.2c01675
ACS Appl. Energy Mater. 2022, 5, 10056−10066

(56) Ao, L. Y.; Du, S. Y.; Yang, J. X.; Jin, C. Q.; Jiang, K.; Shang, L. Y.; Li, Y. W.; Zhang, J. Z.; Zhu, L. Q.; Hu, Z. G.; Chu, J. H. A novel composite of SnO_x nanoparticles and SiO_2@N-doped carbon nanofibers with durable lifespan for diffusion-controlled lithium storage. *J. Alloys Compd.* **2022**, *897*, 162703.
(57) Tan, Y.; Wong, K.-W.; Ng, K. M. Novel Silicon Doped Tin Oxide-Carbon Microspheres as Anode Material for Lithium Ion Batteries: The Multiple Effects Exerted by Doped Si. *Small* **2017**, *13*, 1702614.

https://doi.org/10.1021/acsaem.2c01675
ACS Appl. Energy Mater. 2022, 5, 10056−10066